

Multiscale ab-initio modeling and experiment of nano-CaCO₃ and fiber synergy on toughening low-carbon geopolymers composites

Li Li ^{a,b}, Zhili Ma ^b, Xing Ming ^{c,*}

^a Key Laboratory of Agricultural Soil and Water Engineering in Arid and Semiarid Areas of Ministry of Education, Northwest A&F University, Yangling 712100, China

^b College of Water Resources and Architectural Engineering, Northwest A&F University, Yangling 712100, China

^c Institute of Applied Physics and Materials Engineering, University of Macau, Avenida da Universidade, Taipa, Macao SAR, China



ARTICLE INFO

Keywords:

Nano-calcium carbonate
Polyethylene fiber
Synergistic toughening effect
Geopolymer
Ab-initio modeling

ABSTRACT

Although the geopolymers are generally regarded as a solution to low-carbon building materials, the intrinsic high brittleness greatly limits its further engineering practices. Here, we performed multi-scale ab-initio modeling and experiment on synergistic effect of nano-calcium carbonate (NCC) and polyethylene fiber (PEF) on toughening mechanisms of geopolymers for the first time. Results showed that NCC significantly improved microscale geopolymers gels aggregation on the surface of PEF through the nano-scale calcium (Ca)-triggered electrostatic attractions and high bonding between N/CASH-polyethylene. Due to micro-scale gel aggregation, meso fiber dispersion, geopolymers with 12 mm + 6 mm PE fiber + 1% NCC showed the best synergistic effect on macro-scale bending toughness and multiple cracking characteristics. The relationship of fiber reinforcing index-toughness, toughness-crack amount and toughness-crack fractal dimension tracked good linear, natural log and exponential function, respectively. The crack number and crack fractal dimension are applicable visible indicators of the bending toughness of PEF reinforced GCs.

1. Introduction

Concrete is the most common man-made building material, and the Portland cement is the most widely used binding material for making concrete. Nevertheless, the production of Portland cement leads to a huge energy consumption and emission of CO₂. E.g., 0.66–0.82 kg of carbon emissions are generated in the production of 1 kg of ordinary Portland cement, which accounts for 5%–7% of anthropogenic CO₂ emissions [1]. On the other hand, the high temperature of 1400 °C in the production process of Portland cement consumes a lot of energy. Therefore, the research and development of low energy consumption and high eco-friendly new cement have caught much attention in the field of global building materials research. Among various attempts, the geopolymers composite (GC) is a favorable alternative for Portland cement and can realize a 9–64% decrease in the complete carbon emission [2]. Moreover, the industrial, agricultural and construction wastes, such as fly ash, slag, rice husk ash, waste glass, waste concrete etc. can be recycled in the process of manufacturing GC, thus benefiting the environmental issues.

Unfortunately, similar with Portland cement-based composites, GC are also highly brittle or even more brittle than Portland cement-based

materials [3]. So various kinds of fibers are used in Portland cement-based composites and GC for cracking resistance and toughening [4–13]. Nonetheless, these cracks start from micro-scale cracks and defects in the matrix, making them difficult to be controlled by incorporating macroscopic fibers alone [13]. Therefore, nanomaterials and macroscopic fibers are combinedly used in cement-based materials to demonstrate multi-scale reinforcing roles and further improve the mechanical properties and durability of cement-based materials [14]. Lei et al. [15] used both nano-silica fume and polyethylene fiber (PEF) to prepare the ultra-high strength and ultra-high toughness concrete. The incorporation of nano-silica fume increased the hydration product attached on the surface of PEFs and decreased the size of interfacial transition zone between fiber and matrix. The use of 0.4 wt% nano-silica fume and PEF produced an ultra-high-performance concrete with the saturated multi-crack ductility of 6.53% and compressive strength of 163 MPa. Wu et al. [16] employed both nano-SiO₂ and steel fiber to produce ultra-high strength concrete, where the optimized nano-SiO₂ volume fraction was 1%. The enhancement on bond properties between steel fiber and matrix was related to the denser interface, tight bonding and higher strength of hydration products after introducing nano-SiO₂.

Although the microstructure of GC is quite different from that of Portland cement matrix composites, e.g., the main gel in Portland

* Corresponding author.

E-mail address: yc07806@um.edu.mo (X. Ming).

Nomenclature

ASPC	always stable predictor corrector
C-A-S-H	calcium-aluminosilicate-hydrates
CDD	charge density difference
C-S-H	calcium-silicate-hydrate
DFT	density functional theory
DZVP	double- ζ Valence Polarized
EDS	energy dispersive spectroscopy
FTIR	fourier transform infrared spectroscopy
GC	geopolymer composite
GPW	Gaussian plane wave

GTH	Goedecker-Teter-Hutter
N-A-S-H	sodium-aluminosilicate-hydrates
NCC	nano- calcium carbonate
OT	orbital transformation
PBE	Perdew-Burke-Ernzerhof
PEF	polyethylene fiber
PVA	polyvinyl alcohol
SEM	Scanning electron microscope
SCF	self-consistent field
TGA	Thermogravimetric analysis
γ	synergistic effect coefficient
β	relative enhancement coefficient

cement-based materials is calcium silicate hydrate (C-S-H), while the main gel in GC is sodium- or calcium-aluminosilicate-hydrates (N/C-A-S-H), the nanomaterials can still be employed to reinforce the GC. The use of 0.35 wt% in-situ reduced graphene oxide increased the bending strength, Young's modulus and toughness of fly ash based GC by 134%, 376% and 56%, respectively [17]. The incorporation of nano-TiO₂ increased the compressive, bending strength, and bending to compressive strength ratio, and reduced the shrinkage of slag-based GC [18]. The addition of 1.0–2.0 wt% nano- calcium carbonate (NCC) improved the bending, compressive strength, hardness and dynamic property of fly ash-based GC [19]. In addition, the cost of NCC is lower than that of graphene oxide, nano-TiO₂ and other nanomaterials, so it has more application potential.

However, due to the limitation of scale, it is difficult for a single nanoparticle to limit the crack resistance and improve the toughness of GC on macro scale. For example, the individual nano-SiO₂ cannot improve the bending strength of GC concrete. Nevertheless, when nano-SiO₂ is employed with steel fiber, bond strength, bending properties and fracture properties of GC concretes were improved considerably [20]. Zhang et al. [21] used numerical modeling to study the rebar-matrix bond properties of GC materials modified by nano-SiO₂ and polyvinyl alcohol fiber. Simultaneous use of 0.6%-0.8% PVA fiber and 1.5%-2% nano-SiO₂ enhanced the bond strength and toughness of the GC composites significantly. The addition of NCC could improve the bending,

compressive strength, hardness and dynamic property of GC [19]. However, it is not clear whether the simultaneous use of NCC and fiber can produce positive hybrid effects and improve the toughness of GC.

GC is a multi-scale material, so the toughening mechanism of GC by nano-materials and fibers needs to be studied from multi-scale view. Nonetheless, the existing studies mainly focus on macroscopic mechanical properties [22]. The insightful strengthening and toughening mechanisms of nanomaterials and macroscopic fibers on GC are rarely studied from through the multi-scale footprint (i.e., the macro-, meso-, micro- and nano-scale). To that end, the multiscale ab-initio modeling and experiments were conducted on the GC materials modified by NCC and PEF, where the synergistic effect of NCC and PEF on toughening GC was uncovered. In details, the nano-scale interactions among GC hydrates, PEFs and NCC were revealed through ab-initio modeling. Subsequently, the microstructure and phases assemblages at micro-scale were observed and determined by Scanning electron microscope (SEM), energy dispersive spectroscopy (EDS), Thermogravimetric analysis (TGA) and Fourier Transform Infrared Spectroscopy (FTIR) to verify the former ab-initio calculations. Finally, the features of PEF dispersion were studied in meso scale to analyze the macro- scale bending toughness index and crack properties. Based on the above the multi-scale investigation, it's hoped to give a deep insight into toughen mechanisms of nanomaterials and fibers on GC and facilitate their engineering practices.

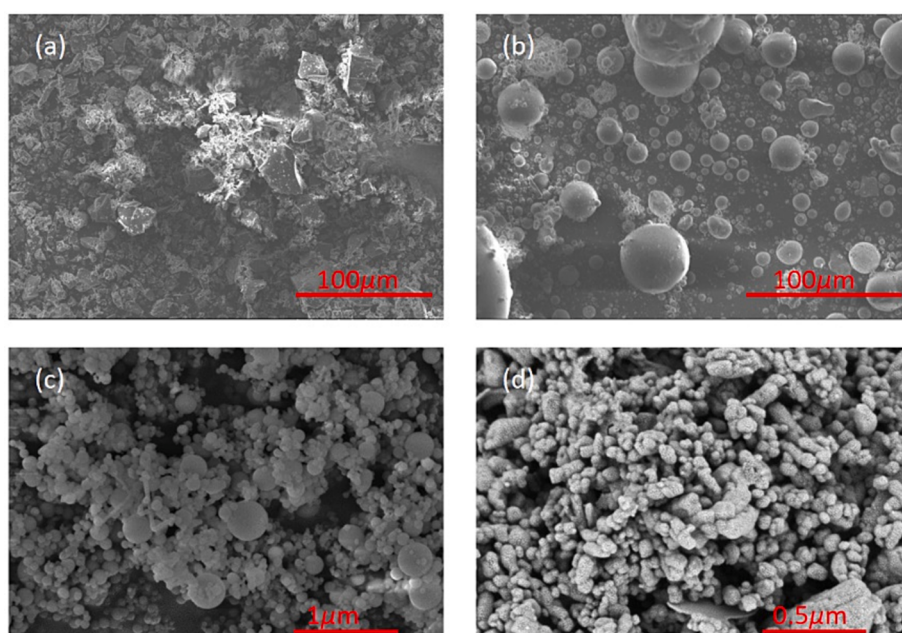


Fig. 1. SEM morphologies of (a) slag, (b) fly ash, (c) silica fume, and (d) NCC.

Table 1

Chemical compositions of raw materials as wt.%.

Composition	CaO	SiO ₂	Al ₂ O ₃	Fe ₂ O ₃	MgO	K ₂ O	SO ₃	Na ₂ O
Fly ash	5.97	52.84	25.65	6.07	1.10	1.72	2.61	1.49
Slag	35.40	35.08	14.92	0.92	7.52	0.49	2.35	1.36
Silica fume	0.47	95.94	0.17	0.02	0.46	0.79	1.16	0.30

2. Materials and methods

2.1. Ab-initio calculations and model construction

Ab-initio calculations were conducted using the density functional theory (DFT) method with the Perdew-Burke-Ernzerhof (PBE) exchange-correlation functional [23,24] as implemented in CP2K/Quickstep [25]. Besides, a hybrid Gaussian plane wave (GPW) scheme was used to describe the atomic orbitals and re-expand the electron density in the reciprocal space [26]. The wave function optimization and self-consistent field (SCF) convergence were accelerated by using the orbital transformation (OT) method [27] accompanied with a wave function extrapolation strategy of always stable predictor corrector (ASPC). The 1 s electron of H, 2 s, 2p electrons of O and C, 3 s, 3p electrons of Al and 3 s, 3p, 4 s electrons of Ca were treated as valance electrons, and the rest core electrons were described by Goedecker-Teter-Hutter (GTH) pseudopotentials [28,29]. We employed a molecularly optimized double- ζ Valence Polarized (DZVP) basis set for expanding Kohn-Sham orbitals [30] and a 400 Ry plane wave energy cutoff. Due to the large size of the simulation cell ($30 \times 30 \times 30 \text{ \AA}^3$), the Brillouin-zone integrations were solely sampled with a Γ point. The main gels of the GCs studied in this modeling were C-S-H, C-A-S-H and N-A-S-H. To simplify the complex and poorly crystalline structure of C-S-H for DFT calculations, isolated polymer chains were separated from the nearest crystalline species, tobermorite (14 Å) [31]. The resulting C-S-H phases exhibited a $\text{Si(OH)}_3[\text{Si(OH)}_2]_3\text{Si(OH)}_3$ (C-S-H pentamer) composition. The N/C-A-S-H phase was obtained by replacing bridging SiO_4 units with AlO_4 , further making the composition of $\text{Si(OH)}_3\text{Si(OH)}_2\text{Al(OH)}_2\text{Si(OH)}_2\text{Si(OH)}_3$ [31,32]. To address the effect of NCC on the composition of the interfacial interactions between PEFs and GC gels (Ca enrichment on the PEF surface, detected via energy-dispersive spectroscopy (EDS) and this will be discussed in the following sections), an additional Ca atom replaced two H atoms in the chains, simulating different protonation states of C-S-H and N/C-A-S-H induced by NCC. The PEF was represented as an ethylene tetramer with hydrogen saturation at both ends ($\text{CH}_3(\text{CH}_2)_2\text{CH}_3$). Consequently, four models were generated to compare the bonding performance between GC gels and PEF, namely CSH-PE, CSH-Ca-PE, N/CASH-PE, and N/CASH-Ca-PE.

2.2. Materials

In this paper, the raw materials used to prepare GC are as follows. NCC is produced by Macklin Biochemical Technology Co., LTD., Shanghai, China, with a particle size of 50 nm. Sodium hydroxide is produced by Guangdong Guanghua Sci-Tech Co., Ltd. with the relative apparent density of 2.13 and the purity of $\geq 96\%$. Municipal water is produced by Yangling Xinhua Water Co., Ltd. and the intermediate sand is produced by the ISO Standard Sand Co., LTD., Xiamen, China with particle size of 0.5–1.0 mm, as presented in Fig. 1(a). Sodium silicate solution is produced by Changlong Sodium Silicate Plant, Gongyi, China. The apparent density of sodium silicate is 2.61 g/cm^3 , where the mass fraction of Na_2O and SiO_2 are 9.0% and 28.08% respectively, and the modulus is 3.22. Fly ash is produced by Weihe Power Plant, Shaanxi, China, with an apparent density of 2.3 g/cm^3 , as presented in Fig. 1(b). S95 granulated blast furnace slag powder is produced by Delong Powder Engineering Materials Co., LTD., Xi'an, China, with an apparent density of 2.8 g/cm^3 , as presented in Fig. 1(c). Silica fume is produced by Henan

Table 2

Physical properties of PEFs.

Density (g/cm^3)	Tensile strength (MPa)	Modulus of elasticity (GPa)	Ultimate elongation (%)	Length (mm)	Diameter (μm)
0.97	3360	115	3.5	6, 12	21.7

Table 3Mixing ratio of NCC and PE in GC (kg/m^3).

Group	PEF		NCC
	12 mm	6 mm	
12F0-6F0-N0	0.00	0.00	0.00
12F0.3-6F0-N0	3.91	0.00	0.00
12F0-6F0.3-N0	0.00	3.91	0.00
12F0.6-6F0-N0	0.00	6.82	0.00
12F0-6F0.6-N0	0.00	0.00	15.63
12F0-6F0-N1	0.00	0.00	30.55
12F0-6F0-N2	6.82	0.00	0.00
12F0.3-6F0.3-N0	3.91	3.91	0.00
12F0.6-6F0.3-N0	6.82	3.91	0.00
12F0.3-6F0.6-N0	3.91	6.82	0.00
12F0.6-6F0.6-N0	6.82	6.82	0.00
12F0.3-6F0.3-N1	3.91	3.91	15.63
12F0.6-6F0.3-N1	6.82	3.91	15.63
12F0.3-6F0.6-N1	3.91	6.82	15.63
12F0.6-6F0.6-N1	6.82	6.82	15.63
12F0.3-6F0.3-N2	3.91	3.91	30.55
12F0.6-6F0.3-N2	6.82	3.91	30.55
12F0.3-6F0.6-N2	3.91	6.82	30.55
12F0.6-6F0.6-N2	6.82	6.82	30.55

Note: In No. 12Fx-6Fy-Nz, x represents long (12 mm) PEF volume fraction, y represents short (6 mm) PEF volume fraction and z represents NCC weight fraction.

Dingnuo Purification Material Co., LTD., Gongyi, China, with an apparent density of 2.0 g/cm^3 , as presented in Fig. 1(d). Chemical compositions of raw materials were tested by X-ray fluorescence spectrometer, as shown in Table 1. The physical properties of 6 mm and 12 mm length PEF produced by Dongguan Sheng Xin Special Rope Factory Co., LTD. are listed in Table 2.

2.3. Mix procedure and specimen fabrication

In this paper, the water-binder ratio (the ratio of the mass of water to the sum of the mass of fly ash, slag and silica fume) is 0.40 and the sand-binder ratio (the ratio of the mass of sand to the sum of the mass of fly ash, slag and silica fume) is 0.2. The alkali activator is sodium silicate combined with solid sodium hydroxide with a modulus of 1.5. By changing the volume dosage and length of PEF and NCC dosage, a total of 19 experimental groups are formulated and listed in Table 3, where the volume fractions of PEF are 0, 0.3%, 0.6%, 0.9% and 1.2%, and the mass contents of NCC are 0, 1% and 2%.

The mixing process of GC is presented in Fig. 2. After mixing, the GCs were cast into plastic molds and vibrated for 60 s. Then the GC specimens were covered by a polymer plastic film for 24-hour curing. Subsequently, the hardened PEF reinforced GCs were demolded and cured in 20°C water tanker for another 27 days according to the ISO 679-2009 standard.

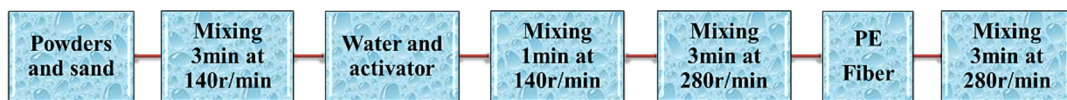


Fig. 2. Mix procedure of fresh GC.

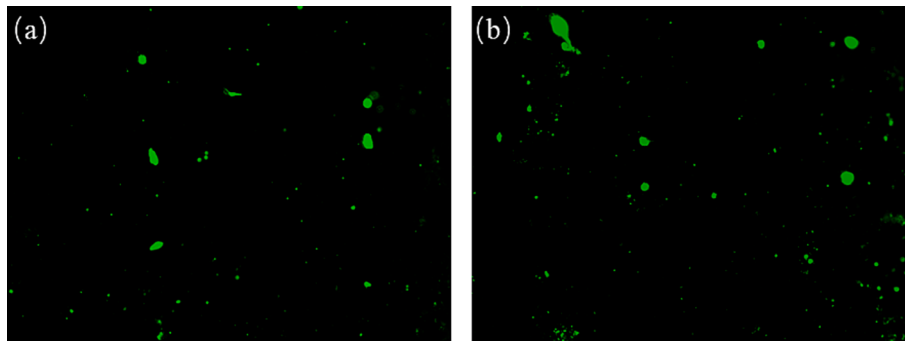


Fig. 3. Fluorescence image of PEF reinforced GC. (a) 12F0-SP0.3-N0 and (b) 12F0.3-SP0-N0.

2.4. Mechanical test of hardened GC

Four-point bending test was carried out on a 40 mm × 40 mm × 160 mm specimen with a span of 120 mm to obtain the bending load–deflection curve and toughness. Three specimens were tested in each group.

2.5. Dispersion of PEF in hardened GC

Obviously, in addition to the physical and mechanical properties of fiber and matrix, the mechanical properties of fiber reinforced composites are mainly controlled by two factors, one is the bond between fiber and matrix, the other is the dispersion of fiber in matrix [15]. In this paper, fluorescence microscopy was used for the first time to study the dispersion of PEFs in GCs. Fig. 3 shows the fluorescence microscopic images of the 426 μm × 321 μm region on the cross-section of different bending specimens. The larger green spots are fibers, and the smaller ones are small PE particles sliding off the surface of the fibers in cutting process. The fluorescence images were transformed into binarization images, and the statistical results were obtained after cleaning. The dispersal factor α can be calculated through eq. (1) [15]:

$$\alpha = \exp \left[-\sqrt{\frac{\sum(\frac{x_i}{x_{\text{average}}} - 1)}{n}} \right] \quad (1)$$

where, x_i is the number of PEFs in the i th image, x_{average} is the average number of PEFs in all images, and n is the number of images. The PEF distribution is more homogeneous when the PEF distribution coefficient is closer to 1 and vice versa.

PEF effective utilization percentage η was evaluated by the ratio of the actual number of PEFs per unit area and was calculated as following.

$$\eta = A/T \quad (2)$$

where η is the effective utilization percentage of PEF and a closer value to 1 shows a more uniform PEF dispersion. A is the actual number of PEFs per unit area and T is the number of PEFs per unit area and can be calculated from eq. (3):

$$T = CV_f/A_f \quad (3)$$

where C is the PEF orientation coefficient. If the PEF is uniformly distributed, the C is 0.5. V_f is the PEF amount, A_f is cross-sectional area of

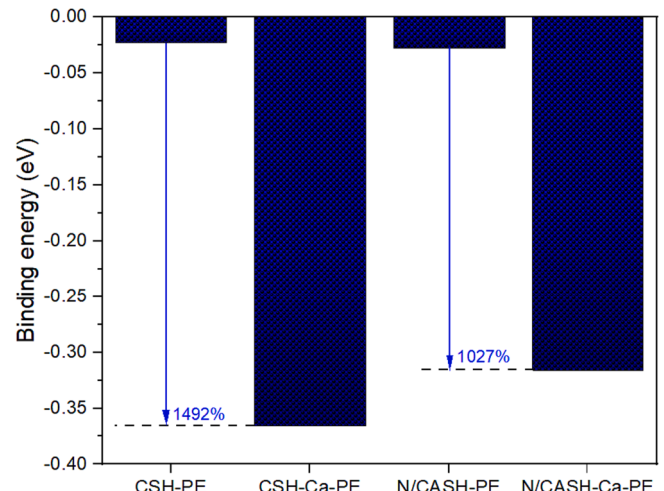


Fig. 4. Binding energy between N/C-(A)-S-H and PEFs with and without Ca.

a individual PEF ($A_f = \pi d_f^2/4$) and d_f is the PEF diameter.

2.6. Microstructure of hardened GC

The SEM was used to observe the morphology of broken specimens after mechanical test. The element composition of PEF surface was obtained by EDS. In addition, the phase assemblages of GC were determined by FT-IR (Agilent Technologies Cary 630 FTIR). Thermogravimetric analysis (TGA) test was carried out under nitrogen gas environment. The GC powder specimens were heated from 30 to 1000 °C with a heating rate of 10 °C/min, being weighed by aluminium oxide tray.

3. Results and discussions

3.1. Nano-scale ab-initio modeling

3.1.1. Binding energy

The binding energy between N/C-(A)-S-H and PEFs was calculated and compared with that modified by NCC (with Ca insertion). Lu et al. [33] indicated that the use of graphene oxide improved the binding energy between C-S-H and PE interface significantly (12% increase in

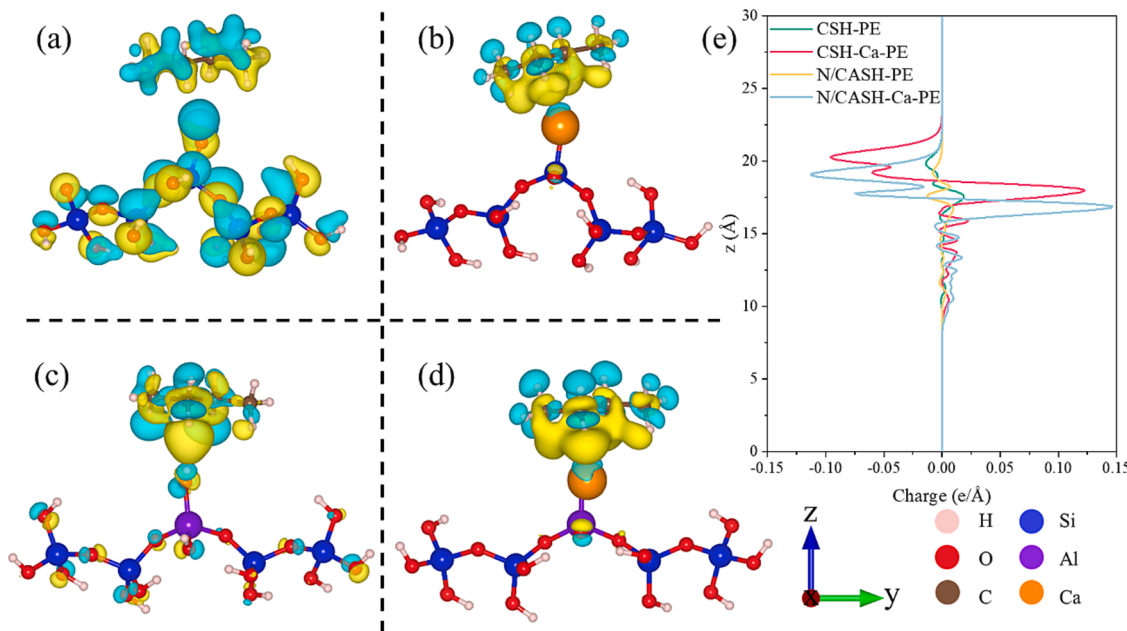


Fig. 5. Charge distribution and CDD of different interfacial models. (a) Charge distribution of CSH-PE (isosurface value 0.1 e/bhor^3), (b) charge distribution of CSH-Ca-PE (isosurface value 0.0015 e/bhor^3), (c) charge distribution of N/CASH-PE (isosurface value 0.0002 e/bhor^3), (d) charge distribution N/CASH-Ca-PE (isosurface value 0.001 e/bhor^3) systems and (e) CDD of different models.

binding energy). Similarly, the Ca^{2+} also improves the binding of C-S-H and N/C-A-S-H with PEF as presented in Fig. 4. The binding energies of CSH-PE and N/CASH-PE interface are both about -0.025 eV . With the introduction of Ca^{2+} , the binding of CSH-PE and N/CASH-PE interfaces are enhanced by three orders of magnitude (1492% and 1027%, respectively). In this situation, it is interesting to find the binding energy of N/CASH-Ca-PE is slightly lower than that of CSH-Ca-PE, which means the interactions between N/C-A-S-H and PEF are weaker than those between C-S-H and PEF, thus benefiting the toughening effect of PEF on GC through fiber slip [34]. Concentrating the underlying reasons, it's probably due to the negative charges induced by incorporation of Al can partially compensate the positive charges of Ca and reduce its electrostatic attraction with PE chains. In general, the cheaper NCC can be used as an alternative to graphene oxide to enhance the toughening effect of PEF, especially in GC matrix.

3.1.2. Electronic properties

The electronic properties of these interfacial models were further calculated to reveal the mechanisms of Ca on improving the bonding between PEFs and GC gels (Fig. 5). The hydrogen bonds are rarely formed during the geometry optimization process due to the lack of polar groups of PE polymer chains, which is greatly different from that between C-S-H and polyvinyl alcohol (PVA) fibers with a hydrophilicity characteristic [35]. When compared the macroscopic properties between PVA fiber reinforce GC and PEF reinforce GC, it is usually found that the latter demonstrate lower strengths but higher tensile ductility [34], which highly depends on the fiber pull-out behavior during the cracking process. The lower bonding between PEFs and N/C-A-S-H (discussed above) and rarely formed hydrogen bonds significantly contribute to slip-hardening responses of PEFs in GC matrix.

We further focused on the charge re-distribution during the binding process. With the introduction of Ca, there are larger charge accumulation and charge depletion areas at the interface region (Fig. 5). Specifically, without Ca, the charge density difference (CDD) at the interface region (projected to z axis) of CSH-PE and N/CASH-PE are both about -0.01 to $0.01 \text{ e/}\text{\AA}$. With the introduction of Ca, the CDD at the interface region are both increased by >10 times to about $-0.1 \sim 0.12 \text{ e/}\text{\AA}$ for CSH-Ca-PE and N/CASH-Ca-PE. After quantitatively calculating

Table 4
Frame charges of different interfacial models.

Models	Frame charges		
	N/C(A)SH	PE	Ca
CSH-PE	-0.007	0.007	N/A
CSH-Ca-PE	-1.406	0.048	1.359
N/CASH-PE	0.002	-0.002	N/A
N/CASH-Ca-PE	-1.471	0.017	1.454

Note: Negative value means charge gain and vice versa. N/A means not applicable.

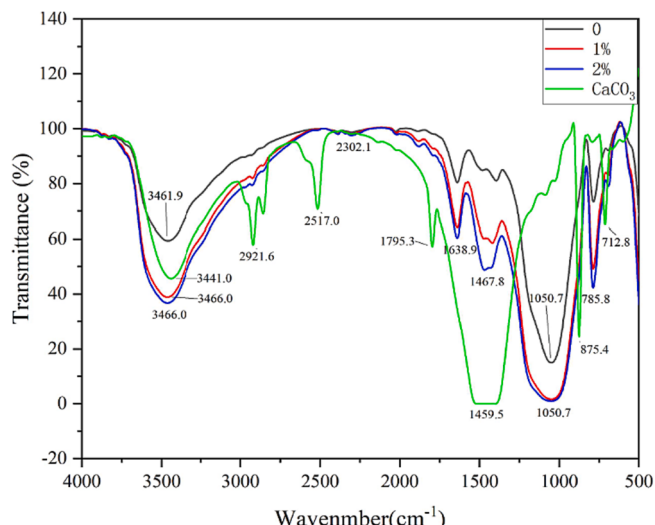


Fig. 6. Infrared spectra of NCC and NCC modified GC.

the charges of different frames (Table 4), it can be found the Ca enhances the charge transfer between the N/C-(A)-S-H and PE, thus improving the toughening effect of PEF on GC matrix. This is consistent with the results of binding energy and the experiments results in section 3.2 and section

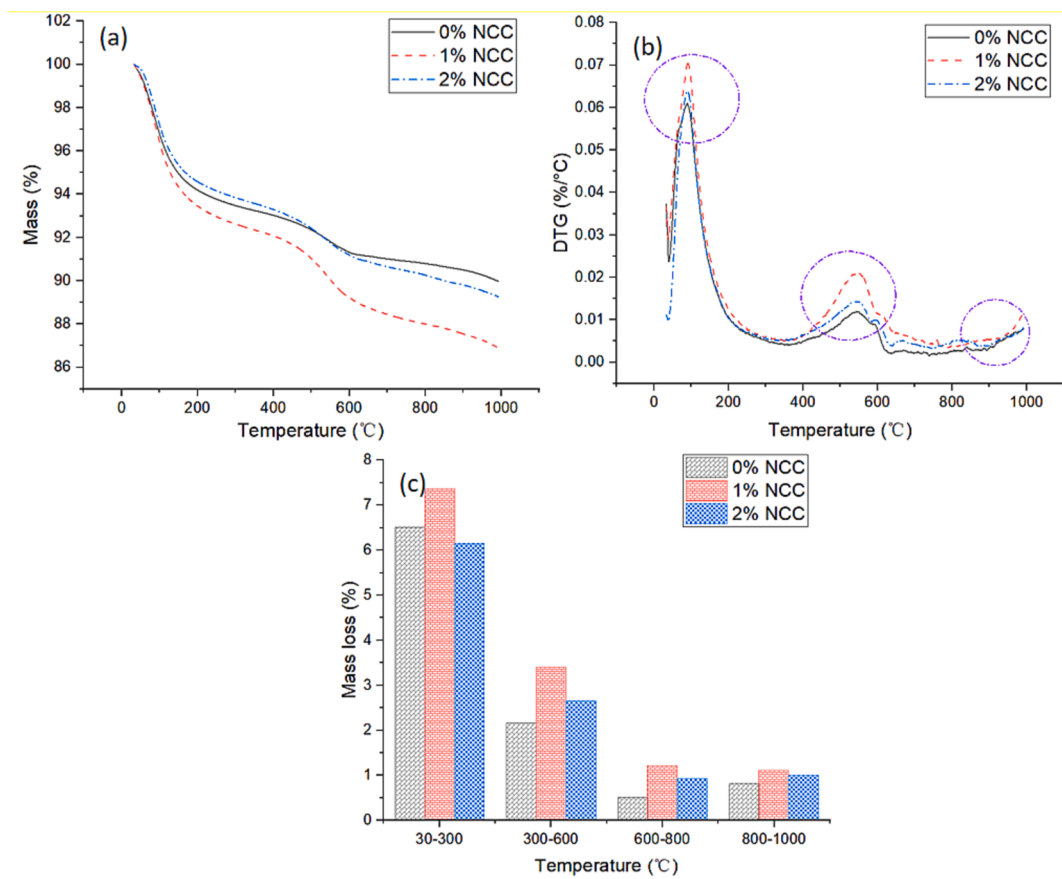


Fig. 7. TGA result of GC with various content of NCC.

3.5.

3.2. Micro-scale structure

3.2.1. FT-IR of matrix

Fig. 6 shows the infrared spectra of NCC modified GC. One of the main absorption peaks of GC with 1% and 2% NCC locate at about 3466 cm^{-1} , which is from the stretching vibration mode of O-H bond in water molecules. The value of this absorption peak is increased with the increase of NCC content, indicating that more water molecules are brought into GC by NCC. The absorption peak at 1468 cm^{-1} is increased with the addition of NCC, which is related to the stretching of carbonate in NCC. This indicates that NCC may be involved in the formation of GC networks [19]. The absorption peak of 1050.7 cm^{-1} is also increased with the addition of NCC, which is a typical peak of alkali-activated GCs and is related to the asymmetric stretching of Si-O-Al. This demonstrates an increase in the amount of geopolymers products.

3.2.2. Thermogravimetric analysis (TGA) of matrix

The TGA of GCs with various content of NCC are illustrated as Fig. 7. The variation of GC specimen mass with the increase of temperature in the range of 30–1000 °C is presented as Fig. 7(a). The key temperature ranges in the DTG chart have been circled in Fig. 7(b). The mass loss ratio in these circled temperature ranges, linked to the various reaction products, as presented in Fig. 7(c). The low temperature mass loss in the range of 40–150 °C is corresponding to the evaporation of physically bound and free water in GC, in which a large mass loss is reached [36]. The water corresponding to N-A-S-H gel is eliminated entirely up to 300 °C [37,38]. The reason is that fly ash accounted for 70% of the precursor, while slag accounted for only 10%, so the amount of Ca was small, and the reaction product was mostly N-A-S-H gel. Up to 300 °C,

the mass loss of GC with 1% NCC (7.37%) was higher than those of the GC without NCC (6.52%) and with 2% NCC (6.15%). The low mass loss of GC with 2% NCC confirms that this mass loss is not primarily due to free water.

The 300–600 °C mass loss is resulting from the dehydration of Ca-rich reaction products. The mass loss of GC with 1% NCC was still the highest (3.41%) in the range of 300–600 °C and followed by GC with 2% NCC (2.66%) and without NCC (2.16%). That is, NCC is beneficial to the forming of both N-A-S-H and C-A-S-H gels. While excess NCC (2%) improve the forming of C-A-S-H gels, but harm that of N-A-S-H. The mass loss below 600 °C is an ancillary sign of reaction degree of GC, which was 8.69%, 10.78% and 8.81% for GC with 0, 1% and 2% NCC, respectively. Hence, the reaction degree of GC with 1% or 2% NCC was consistent higher than that of GC without NCC. We can conclude that NCC is beneficial to the reaction of fly ash-slag based GC, while maybe it is better used in GC with C-A-S-H as the main gel.

The mass loss hump in the range of 650–800 °C associates with the decomposition of calcium carbonate into carbon dioxide and calcium oxide. The CaCO_3 phase was also recognized by FTIR test. In the range of 800–1000 °C, significant growth of mass loss was identified in all GC specimens. The mass loss of GC with 1% and 2% NCC in this range are both higher than that without NCC, in line with the forecast, as shown in Fig. 7(c). However, the mass loss of GC with 1% NCC presents higher value than that of GC with 2% NCC, due to the poorer dispersion of NCC and less carbonation products of 2% NCC reinforced GC than those of 1% NCC reinforced GC.

3.2.3. SEM

Fig. 8 shows the scanning electron microscope image of PEF. Before adding into GC, the notch at the end of PEF is basically flat and there are dents on the PEF surface, which benefits the enhancement on the

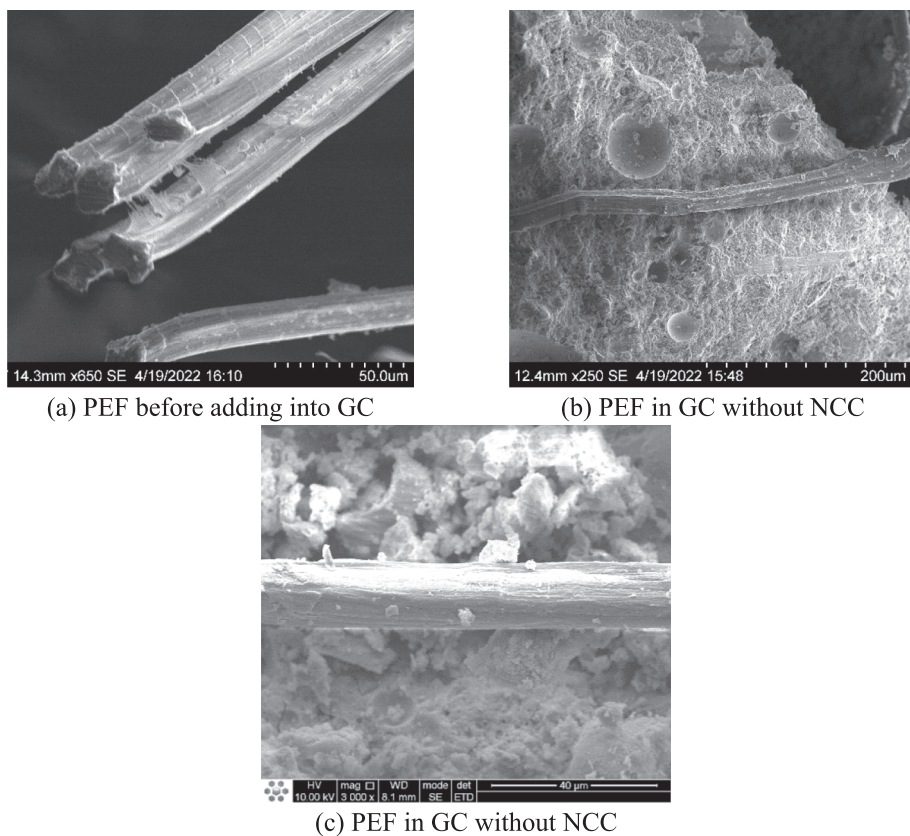


Fig. 8. Morphologies of PEFs. (a) PEF before adding into GC, (b) PEF in GC without NCC, (c) PEF in GC without NCC.

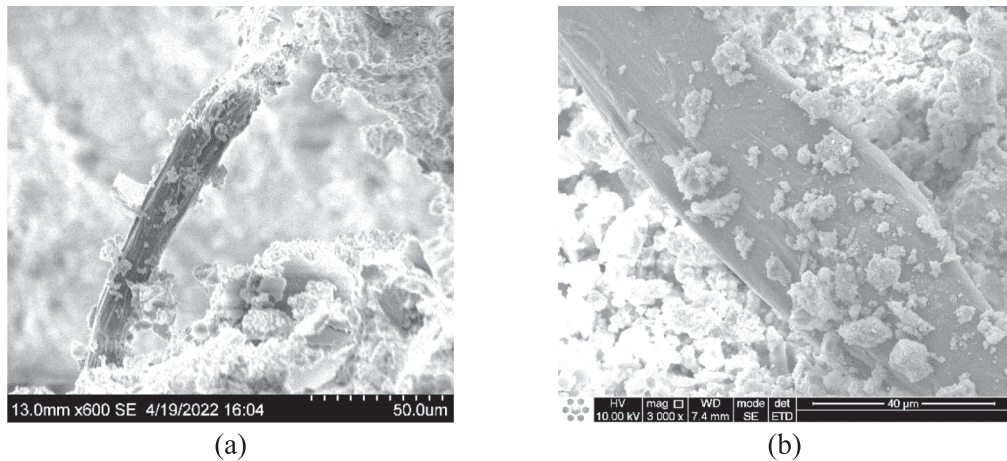


Fig. 9. Morphologies of PEFs in GC with 1% NCC.

bonding between PEF and GC (Fig. 8 (a)). In GC without NCC, there are some GC debris on the surface of PEF, indicating the good bonding between PEF and GC (Fig. 8 (b)). As presented in Fig. 8 (c), at higher magnification, the PEF surface is still flat and smooth. Although the surface of the PEF adhered to the GC matrix fragments, but the number of matrix fragments is small.

As presented in Fig. 9 (a), in GC with 1% NCC, there are more GC debris on the surface of PEF than that in GC without NCC (Fig. 9 (b)). At higher magnification, it is more clearly that the number of matrix fragments on the surface of PEF in the 1% NCC GC (Fig. 9 (b)) was significantly more than that in the non-NCC GC (Fig. 8 (c)). These demonstrates the better bonding properties between PEF and matrix in 1% NCC modified GC than that in non-NCC GC.

As presented Fig. 10 (a), in 2% NCC modified GC, there are much more filaments on the surface of PEF than those in 1% and none NCC modified GC (Figs. 8 and 9). Many PEF filaments can be seen on the surface of the PEF, indicating that the PEF generates a lot of friction force with the matrix when pulled out. Moreover, as presented Fig. 10 (b), there are necking of the ends of PEFs. These indicates that the resistance of matrix is very high, but the excess high bonding may reduce the energy consumption during the PEF pulling out process, leading to the decreasing of toughness of composites [39].

By comparing Fig. 8(c) and Fig. 9(b), it can be found that structure of the matrix product becomes denser after the NCC increases from 0% to 1%, therefore indicating the ideal quantity for the nanoparticles in GC, consistent with TGA results. The introduction of NCC in fly ash-slag

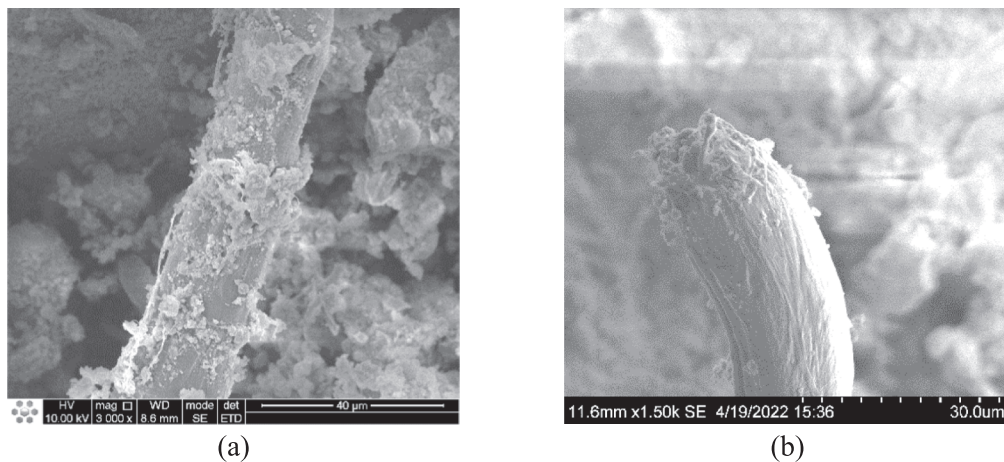


Fig. 10. Morphologies of PEFs in GC with 2% NCC.

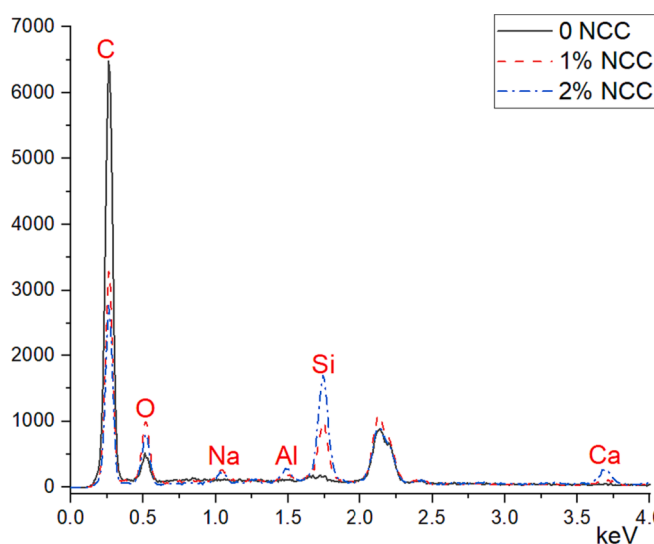


Fig. 11. EDS on PEF surface of GC.

based GC leads to a possible reaction mechanism in the presence of NCC in the geopolymization process [19]. It is probable to accelerate the reaction of alkali-activated fly ash-slag by employing NCC, constituting a further C-(A)-S-H [40]. These C-(A)-S-H around NCC are spread between fly ash and slag particles and work as the seeds to establish denser

GC paste. On the contrary, GC resulted in a slight opposite pattern, displaying lower density, resulting from the insufficient mixing alkaline solution after adding NCC in wake of its higher surface area and lower particle size [19], consistent with TGA test results. The excess water molecules, being brought into GC by NCC, also contribute to this result, as indicated by FTIR in section 3.2.1.

3.2.4. EDS

The corresponding EDS patterns of the areas on PEF surface of Fig. 8(c), Fig. 9(b) and Fig. 10(a) are presented in Fig. 11. The surfaces of PEFs are subject by C, O, Si, Na, Al and Ca. With the introduction of 1% and 2% NCC in GC, the Ca amount on the PEF surface are increased from 0.32 wt% to 0.82 wt% and 2.3 wt%, respectively. With the introduction of 1% and 2% NCC in GC, the Si amount on the PEF surface are increased from 0.80 wt% to 4.48 wt% and 7.70 wt%, respectively. With the introduction of 1% and 2% NCC in GC, the Na amount on the PEF surface are increased from 0.87 wt% to 2.37 wt% and 1.99 wt%, respectively. The Ca comes from NCC and C-A-S-H, Si and Na come from N/C-A-S-H. The increased Si, Al and Na amount on the surface of PEF indicate that NCC induced geopolymers gel aggregation on the fiber surface. Nano-scale Ca-triggered electrostatic attractions and high gel bonding between Ca and N/C-A-S-H, being obtained by ab initio simulation, are the main reasons of these results of SEM and EDS.

The EDS test indicates higher geopolymers products (Si and Al) amount on the surface of PEF in 2% NCC modified GC than that in 1% NCC modified GC, as shown in Fig. 11. While the TGA test presents more geopolymers products (high temperature mass loss) in 1% NCC

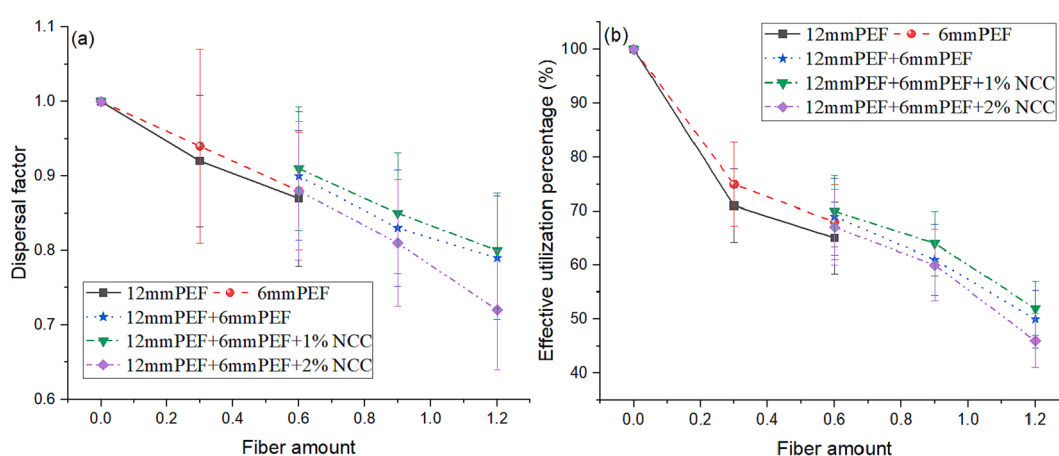


Fig. 12. Impact of PEF amount on (a) dispersal factor and (b) effective utilization percentage.

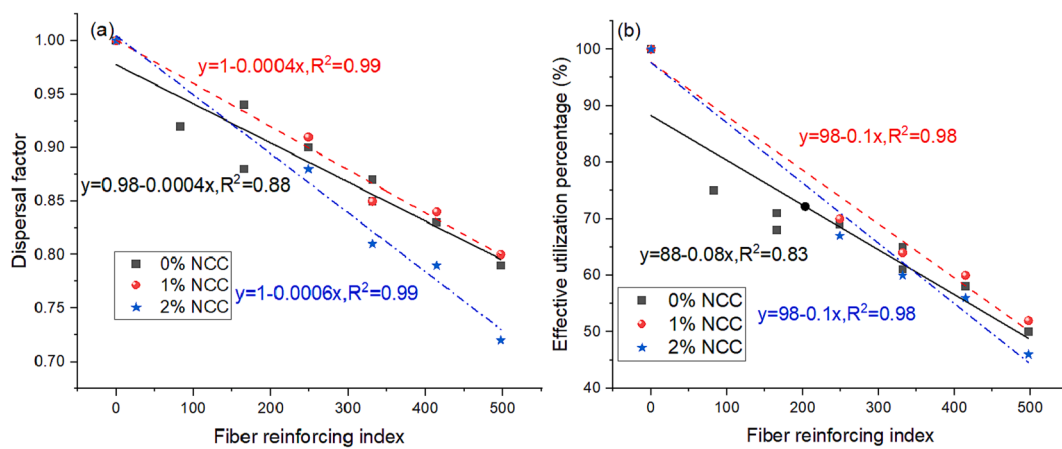


Fig. 13. Impact of PEF reinforcing index on (a) dispersal factor and (b) effective utilization percentage.

Table 5

Regression ANOVA of relation between dispersal factor and PEF reinforcing index.

	DF	Sum of Squares	Mean Square	F Value	P Value
GC with 0% NCC	1	0.0276	0.0276	53.72289	0.00016
GC with 1% NCC	1	0.02378	0.02378	169.16107	0.00098
GC with 2% NCC	1	0.04438	0.04438	215.47328	0.00069

modified GC matrix than that in 2% NCC modified GC matrix, as shown in section 3.4. These phenomena may be due to the fact that the good dispersion of the appropriate amount of NCC (1%) in GC is more conducive to the geopolymmerization reaction.

3.3. Meso-scale fiber dispersion

3.3.1. Impact of PEF amount on PEF dispersion

The macroscopic toughening effect of a kind of fiber on composites mainly depends on two aspects. One is the bonding properties of the fiber-matrix interface [41], which has been discussed above by micro- and nano- scale research. The second is whether the fiber is evenly dispersed in the matrix [42], which determines whether the fiber can normally play the role of crack resistance.

Impact of PEF amount on the PEF distribution is presented in Fig. 12. With the increase of PEF volume fraction, the α and η of PEF are both decreased. When the PEF content is 0.6%, the α and η of long-short hybrid PEF reinforced GC are higher than that of long or short individual PEF reinforced GC regardless of NCC content. This is because that the short PEF can be dispersed among the long PEFs and reduce the probability of PEF agglomeration and balling compared with the use of individual PEF. The introduction of 1% NCC in long and short hybrid PEF reinforced GC increased the α and η of PEF, which originates from the NCC-triggered optimization of gradation of PEFs. Nonetheless, this improvement can be reduced after further incorporation of NCC (e.g., 2%), the α and η of PEF are significantly decreased [43]. The reason for this phenomenon is that the dispersion of the fibers requires a proper range of slurry viscosity [44]. NCC can increase the viscosity of the slurry, 1% NCC is good for fiber dispersion, but 2% NCC is bad for fiber dispersion.

3.3.2. Impact of PEF reinforcing index on PEF dispersion

As discussed above, the fiber dispersion is significantly affected by PEF length except the PEF amount. Hence, the PEF reinforcing index

Table 6

Regression ANOVA of relation between effective utilization percentage and PEF reinforcing index.

	DF	Sum of Squares	Mean Square	F Value	P Value
GC with 0% NCC	1	1293.63333	1293.63333	33.71485	0.00066
GC with 1% NCC	1	1324.98868	1324.98868	124.95445	0.00153
GC with 2% NCC	1	1656.54528	1656.54528	137.07557	0.00134

(product of PEF content and PEF aspect ratio) is introduced to evaluate the coupled effects of PEF content and aspect ratio. As presented in Fig. 13, the α and η of PEF are both decreased with the increase of PEF reinforcing index and a good linear relation is demonstrated between them with high correlation coefficients. All the correlation coefficients are higher than 0.8. As shown in Table 5 and Table 6, all the P -values are less than 0.05, so the regression passes the overall significance test, regression models are meaningful. Hence, PEF reinforcing index is an applicable parameter to measure the toughening effect of PEF on GCs. The combination using of NCC and PEFs in GC leads to a higher decrease in slope than that without NCC, resulting from the viscosity increases of fresh mortar due to NCC.

3.3.3. Synergistic effect on PEF distribution

The synergistic effect of NCC and various PEFs with different lengths on PEF distribution is also evaluated through the following Eq. (4) and (5). The positive synergistic effect is always demonstrated on synergistic effect coefficient with more positive values ($\gamma > 1$).

$$\gamma_{A-B-C} = \frac{\beta_{A-B-C}}{\beta_A \beta_B \beta_C} \quad (4)$$

where, γ_{A-B-C} is the synergistic effect coefficient of the combined actions of A, B and C. β_{A-B-C} is the relative enhancement coefficient under the combined action of A, B and C. β_A , β_B and β_C are the relative enhancement coefficient under the individual action of A, B or C, respectively.

$$\beta = \frac{\alpha}{\alpha_0} \quad (5)$$

where, β is relative enhancement coefficient. α is the experimental data of the individual PEF or NCC reinforced GC. α_0 is the experimental data of the pure GC without PEF or NCC.

Synergistic effect coefficient between NCC and two lengths of PEF on α and η of PEF are also presented in Fig. 14. The positive synergistic effect of α and η is achieved in most groups except the one with 2% NCC.

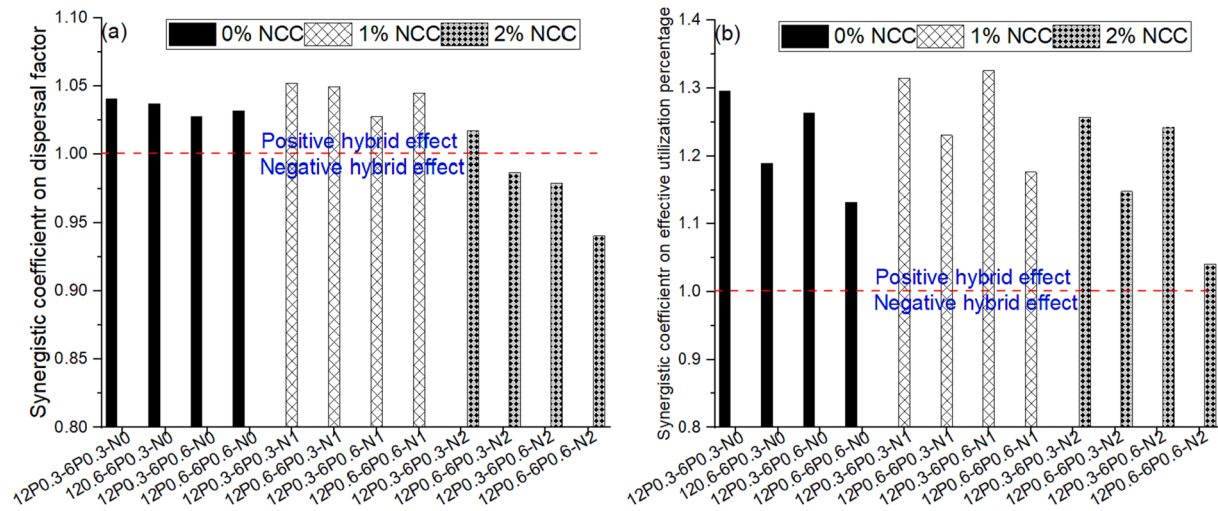


Fig. 14. Synergistic effect coefficient on (a) dispersal factor and (b) effective utilization percentage.

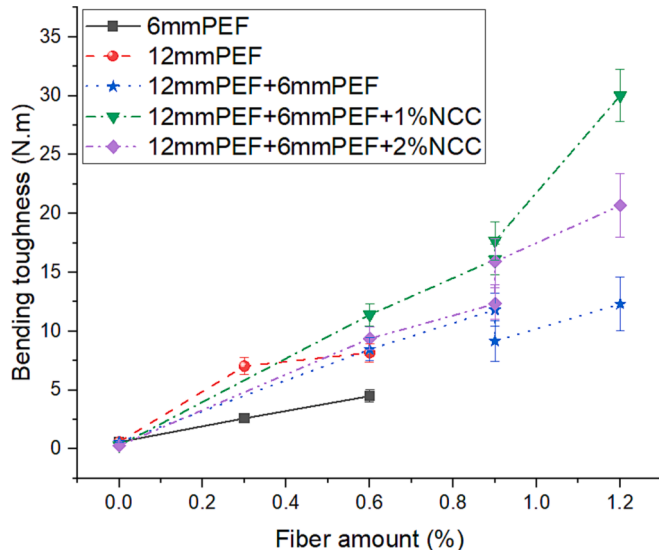


Fig. 15. Impact of PEF amount on the bending toughness.

In addition, the synergistic effect coefficient on α and η of PEF in GC without NCC and 1% NCC are both higher than that in GC without 2% NCC. This result more directly proves that reasonable hybrid of long and short PEFs and PEF-NCC hybrid can improve fiber dispersion. For fiber dispersion, 1% is a reasonable amount of NCC in GC.

3.4. Macro-scale bending toughness

3.4.1. Impact of PEF amount on bending toughness

As presented in Fig. 15, the bending toughness is improved with the increase of PEF volume fraction. Incorporation of NCC alone has no significant effect on bending toughness. The long PEF increases the bending toughness more significantly than short PEF due to its longer length-triggered higher crack bridging capacity. With the addition of 0.6% PEFs both for short and long PEFs, the hybrid scheme of them demonstrates a more enhancement on the bending toughness more significantly than any individual of them, which ascribes to the well packing of short and long hybrid PEFs in GC matrix. This improvement is further enhanced through the hybrid use of them and additional introduction of NCC particles [13,45], originating from the multi-scale enhancement of PEFs and nanoparticles. E.g., for GC with 1% and 2%

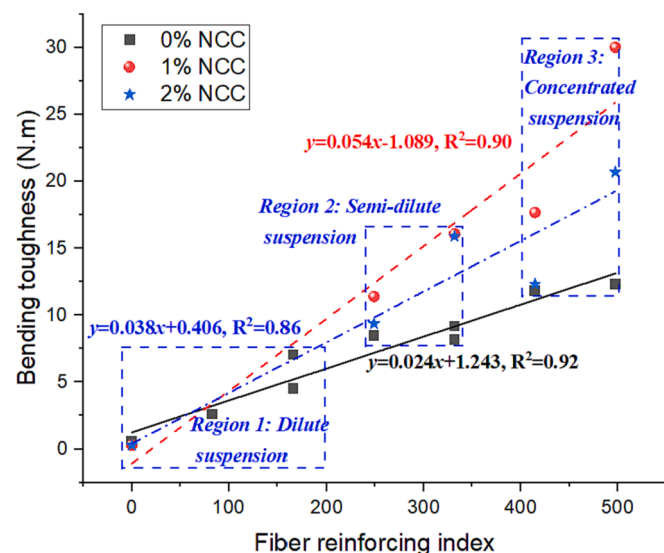


Fig. 16. Impact of PEF reinforcing index on the bending toughness.

NCC, the bending toughness is increased by 663% and 1285% with short and long hybrid PEFs, respectively.

It is interesting to note that, there is a correlation between PEF dispersion and standard deviation of bending toughness data. That is, good fiber dispersion improves the robustness of mechanical properties of fiber reinforced composites [42,44]. The standard deviations of bending toughness are increased with the growth of fiber amount, due to the poor fiber dispersion of high amount PEF, as shown in Fig. 12 of section 3.3. In addition, although the toughness of GC with 1% NCC are higher than those without NCC and with 2% NCC, the standard

Table 7

Regression ANOVA of relation between bending toughness and PEF reinforcing index.

	DF	Sum of Squares	Mean Square	F Value	P Value
GC with 0% NCC	1	117.6516	117.6516	98.16198	0.000023
GC with 1% NCC	1	428.50837	428.50837	37.32136	0.00881
GC with 2% NCC	1	209.32507	209.32507	24.88863	0.01549

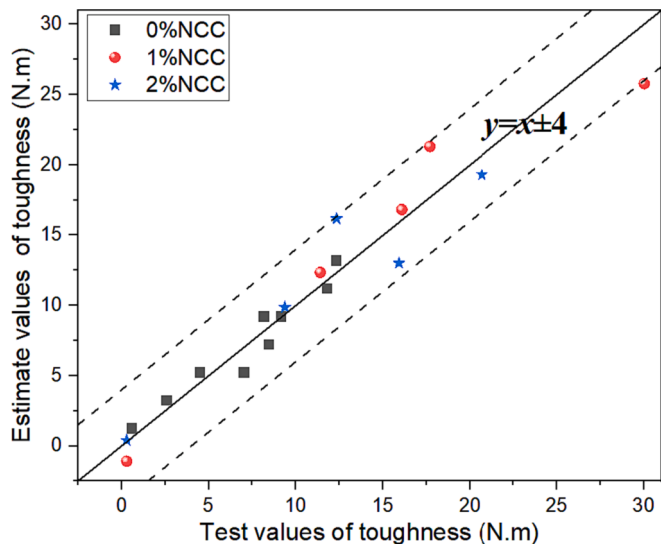


Fig. 17. Test values vs. estimate values of toughness by fiber reinforcing index based on equations in Fig. 7.

deviations of the toughness data of GC with 1% NCC are similar with those without NCC and with 2% NCC. This also due to the better fiber dispersion of GC with 1% NCC than the others, as shown in Fig. 12.

3.4.2. Impact of PEF reinforcing index on bending toughness

As presented in Fig. 16, there is a positive linear relation between bending toughness and PEF reinforcing index with high correlation coefficients of 0.86–0.92. The statistic F of bending toughness of GC with 0, 1% and 2% NCC are 98.16198, 37.32136 and 24.88863, respectively, corresponding P -value are 0.000023, 0.00881 and 0.01549, respectively, as shown in Table 7. All the P -values are less than 0.05 significantly, so linear regression passes the overall significance test, regression model is meaningful. And the results of toughness estimated by the equations in Fig. 16 are all very accurate. The relationship between predicted and measured toughness is in the range of $y = x \pm 4$ (N.m), as shown in Fig. 17. Hence, the liner equations in Fig. 16 can be used for performance-based fiber mix design of GC.

Incorporation of 1% NCC slightly increases the slop of linear function, indicating that NCC facilitates the enhancement on bending toughness. Nonetheless, an adverse effect is demonstrated after introduction of 2% NCC, which means 1% is the optimal content for NCC to improve the toughening effect of PEF on GC. Concerning the responses of bending toughness upon the increased PEF reinforcing index, the values of bending toughness can be generally divided into three regions. When the PEF reinforcing index is smaller than 200, bending toughness locates at 0–7 N.m. When PEF reinforcing index is between 200 and 400, the bending toughness increases to 8–16 N.m. With the further increase in PEF reinforcing index (>400), the bending toughness is finally higher than 10 N.m. Hence, the values of 200 and 400 are the critical and dense PEF reinforcing index for PEF, respectively. Below 200, it corresponds to a dilute suspension area (region 1) and above 400, it corresponds to a concentrated suspension area (region 3). The semi-dilute suspension is just located between them (200–400). As reported by Emdadi et al., the critical and dense fiber reinforcing index of polypropylene fiber in Portland cement mortar were 100 and 300, respectively [46]. The critical and dense PEF reinforcing index value in GC are both higher than those in Portland cement mortar. The reason for this is that the viscosity of GC is higher than Portland cement slurry.

Although the toughness of GC could be predicted by the regression equation in this section. While the more scientific equations should be established in the future based on the PEF-GC bonding strength, the fiber dispersity and orientation factors.

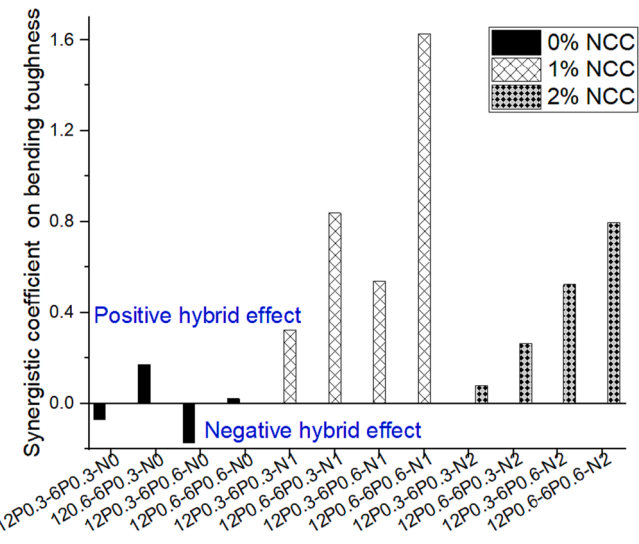


Fig. 18. Synergistic toughening effect coefficient on bending toughness.

3.4.3. Synergistic effect on bending toughness

A combined use of NCC and two lengths of PEFs is conducted to realize the multi-scale enhancement on GCs with multiscale features. In the assistance of synergistic effect factors, the coupled effects of different PEFs and NCC are evaluated [47]. In this paper, the synergistic toughening effect coefficient γ of NCC and PEF with various lengths on bending toughness of GC are calculated by Eq. (6) [47]. The larger the synergistic toughening effect coefficient is, the better the synergistic toughening effect on improving the properties of GC is. Besides, a positive value of the synergistic toughening effect coefficient represents the positive synergistic toughening effect of PEFs and NCC, and vice versa.

$$\gamma_{A-B-C} = \frac{\beta_{A-B-C}}{\beta_A + \beta_B + \beta_C} - 1 \quad (6)$$

where, γ_{A-B-C} is the synergistic toughening effect coefficient of the combined actions of A, B and C. β_{A-B-C} is the relative enhancement coefficient under the combined effect of A, B and C. β_A , β_B and β_C are the relative enhancement coefficient under the individual action of A, B or C, respectively.

$$\beta = \alpha - \alpha_0 \quad (7)$$

where, β is relative enhancement coefficient. α is the bending toughness of the individual PEF or NCC reinforced GC. α_0 is the bending toughness of the pure GC without PEF or NCC.

Synergistic effect coefficient between NCC and two lengths of PEF on bending toughness is presented in Fig. 18. Generally, regardless of NCC content, the group with the lowest PEF content (0.3% long PEF + 0.3% short PEF) has the smallest synergistic toughening effect factor, and 12F0.3-SP0.3-N0 even presents a negative synergistic effect, which means the individual NCC is far from realizing the toughening effect on GC without enough PEFs. The synergistic effect factors of GC with PEF and 1%-2% NCC are higher than those of GC without NCC. All the GCs with NCC realize the macro- scale positive synergistic toughening effect, attributing to the nano-scale NCC-induced enhanced bonding between matrix and PEF, and the meso-scale improved fiber dispersion. In addition, 0.6% long PEF + 0.6% short PEF + 1% NCC reaches the highest synergistic toughening effect in this study, presenting the optimal NCC content of 1% for bending toughness. It is interesting to note that, in Assaedi's research [19], 2% is the optimal content for flexural and compressive strengths, while 1% is the optimal content for impact strength, and hardness.

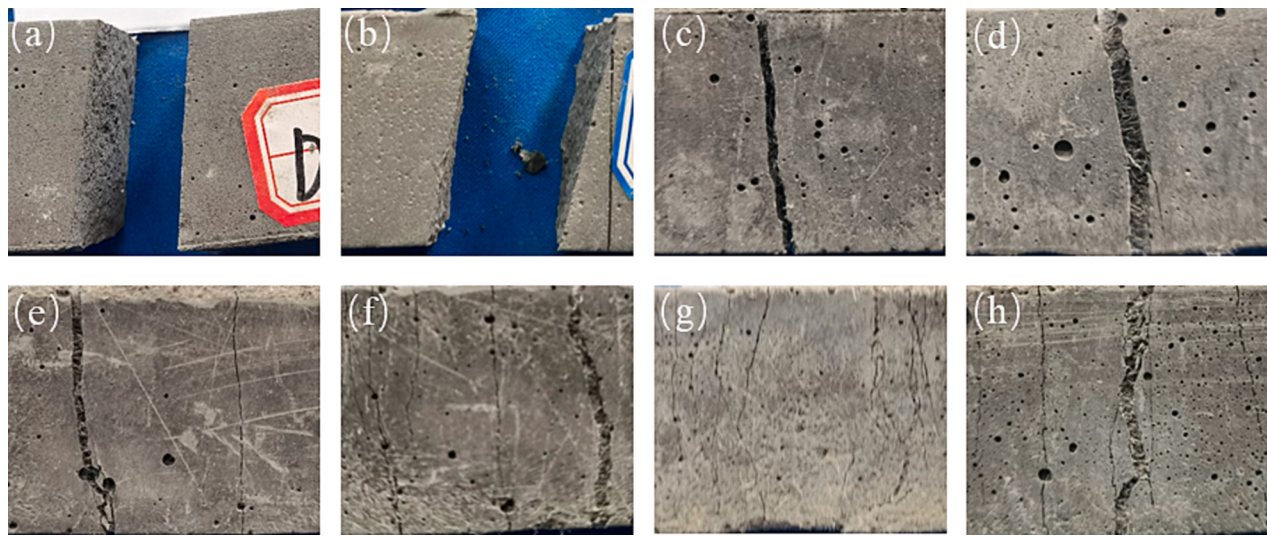


Fig. 19. Crack morphology of GC after bending failure. (a) 12F0-6F0-N0, (b) 12F0-6F0-N2, (c) 12F0-6F0.3-N0, (d) 12F0.3-6F0-N0, (e) 12F0.3-6F0.3-N0, (f) 12F0.6-6F0.3-N0, (g) 12F0.6-6F0.3-N1 and (h) 12F0.6-6F0.6-N2.

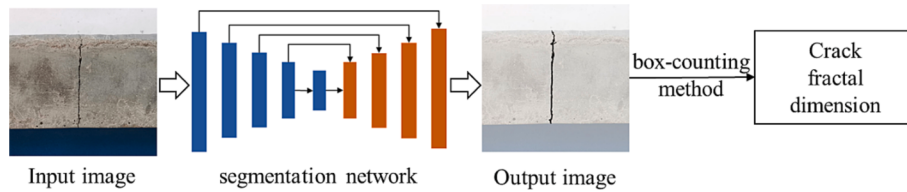


Fig. 20. Crack parameter extraction process [50].

3.5. Macro- scale crack features

3.5.1. Impact of PEF amount on crack features

With the addition of PEF and NCC, the bending toughness of the GC is improved, which further induces the change of bending failure mode (as presented in Fig. 19). For 12F0-6F0-N0, the GC demonstrates obvious brittle failure mode with a flat fracture surface (Fig. 19 (a)). The individual use of NCC is hard to change the brittle failure of GC because it's too small to deflect or bridge the macro-cracks. A main crack presented in the fracture mode of 12F0-6F0.3-N0 has been changed after the addition of PEFs. Due to the existence of PEF, the specimen keeps its integrity after cracking, and demonstrates ductile responses with a secondary crack under tensile load.

Multiple cracks are presented on the surface of 12F0.3-6F0.3-N0,

indicating that the deformation capacity and energy dissipation capacity of the specimen are significantly improved, which is also an important reason for the increase in bending strength. For 12F0.6-6F0.3-N0, the crack number is increased to about 6, which is a typical strain-hardening behavior derived from the positive synergistic effect of long and short PEFs.

For 12F0.6-6F0.3-N1 and 12F0.6-6F0.6-N2, the crack number is further increased to about 10 because of the positive synergistic effect of PEF and NCC. The multi-crack cracking pattern of ultra-high toughness concrete is perfectly realized, consisting with that reported in the literatures [48,49].

It's interesting to find that there is a direct relation between the crack morphology and the mechanical properties of GC. Nonetheless, it is difficult to accurately describe the change of crack morphology only by

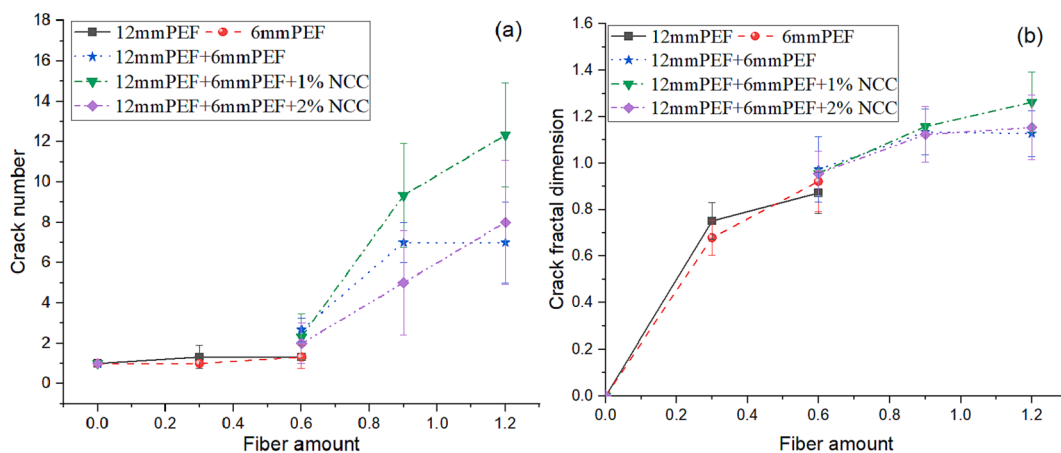


Fig. 21. Impact of PEF amount on (a) crack number and (b) crack fractal dimension.

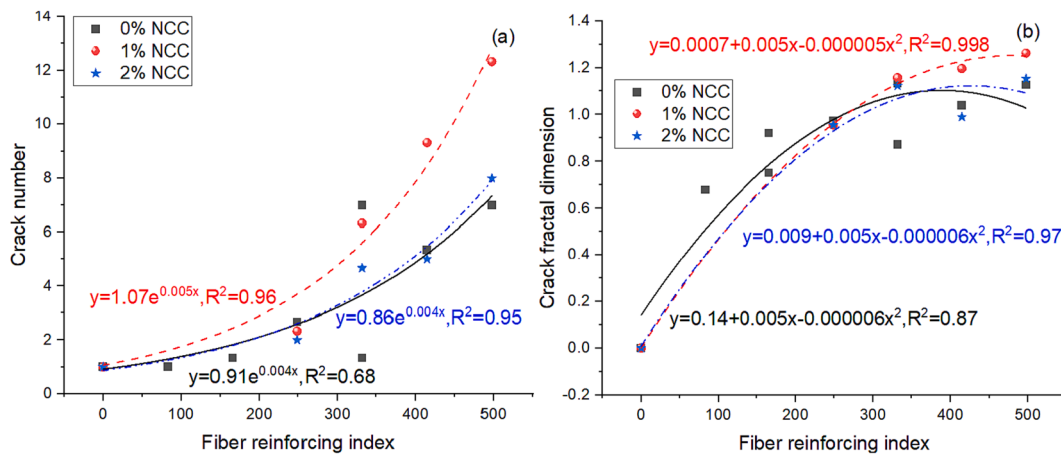


Fig. 22. Impact of PEF reinforcing index on (a) crack number and (b) crack fractal dimension.

the crack number. In order to further quantitatively evaluate the combined effect of PEF and NCC on crack features after failure, the semantic segmentation network using deep learning and image processing methods is developed with capacity of efficiently and accurately extracting the parameters of various types of cracks. The crack multi-parameter extraction process is presented in Fig. 20. The original image is fed into the segmentation network to complete the pixel-level recognition of cracks. The semantic segmentation network consists of an encoding structure (left) for extracting deep-level features in images and a decoding structure (right) for fusing multi-level features. For the sake of the enhancement on the number and variety of data samples, data enhancement methods such as flipping, and color dithering are used.

Fractal dimension can be used to describe the complexity of concrete crack morphology, and box-counting dimension method is used herein to describe the fractal features of cracks quantitatively. Box-counting dimension method is a calculation method to measure the fractal dimension of space. The cracks are placed on evenly divided boxes and the minimum number of boxes needed to completely cover the cracks is calculated. Step by step to reduce the box size, the required change in the number of boxes is recorded. Assuming that the box side length is a , the space is divided into N boxes, and the fractal dimension is defined as follows:

$$\text{Fractal}_{\text{box}}(\text{crack}) = \lim_{a \rightarrow 0} \frac{\lg N(a)}{\lg(1/a)} \quad (8)$$

Impact of PEF amount on the crack number and fractal dimension are presented in Fig. 21. With the increase of PEF volume fraction, the crack number and fractal dimension are both increased. When NCC content is 0 and PEF content is 0.6%, the crack numbers of long and short hybrid PEF reinforced GC are about 2 times of that of long or short individual PEF reinforced GC. The crack fractal dimensions of long and short hybrid PEF reinforced GC are also higher than that of long or short individual PEF reinforced GC. This is because that the combination of long and short PEFs could disperse the stress more evenly and form the multi-crack failure pattern. The introduction of NCC further increases the crack number and fractal dimension. In details, when the PEF content is higher than 0.9%, the crack number and fractal dimension of GC with 1% NCC are higher than that of long and short hybrid PEF reinforced GC without NCC. When the PEF content reaches 1.2%, the crack number and fractal dimension of GC with 1% NCC and 2% NCC are both higher than that of long and short hybrid PEF reinforced GC without NCC, indicating that the use of NCC facilitates the PEF to disperse the stress more evenly and form the multi-crack failure pattern.

3.3.2. Impact of PEF reinforcing index on crack features

Impact of PEF reinforcing index on the crack features is presented in

Table 8
Regression ANOVA of relation between crack number and PEF reinforcing index.

	DF	Sum of Squares	Mean Square	F Value	P Value
GC with 0% NCC	2	123.60024	61.80012	25.02225	0.00065
GC with 1% NCC	2	282.38743	141.19372	124.93744	0.00129
GC with 2% NCC	2	114.36987	57.18494	121.85093	0.00134

Table 9
Regression ANOVA of relation between crack fractal dimension and PEF reinforcing index.

	DF	Sum of Squares	Mean Square	F Value	P Value
GC with 0% NCC	2	0.84321	0.4216	19.55013	0.00235
GC with 1% NCC	2	1.09593	0.54797	592.78507	0.00168
GC with 2% NCC	2	0.89497	0.44749	35.83149	0.02715

Fig. 22. Generally, the relation between crack number and PEF reinforcing index is an exponential function, while the relation between crack fractal dimension and PEF reinforcing index is a quadratic function. As presented in Fig. 22, most of the correlation coefficients are higher than 0.95. As shown in Table 8 and Table 9, all the P -values are less than 0.05, so the regression passes the overall significance test, regression model is meaningful. And the results of crack number and crack fractal dimension estimated by the equations in Fig. 22 are all very accurate, as shown in Fig. 23. Most of the relationships between predicted and measured crack number and fractal dimension are in the range of $y = x \pm 2$ and $y = x \pm 0.2$, respectively. Hence, fiber reinforcing index is an applicable parameter to predict the crack features of PEF reinforced GCs. However, the predictions of crack number and fractal dimension are more discrete than that of bending toughness (in Fig. 21), because the process of crack generation and development has very significant intrinsic randomness [51].

The combination using of 1% NCC, short and long PEFs shows the best enhancement on the crack number and fractal dimension of GC. In general, the variation trend of crack number and fractal dimension is basically consistent with the bending toughness and there is a correlation between them.

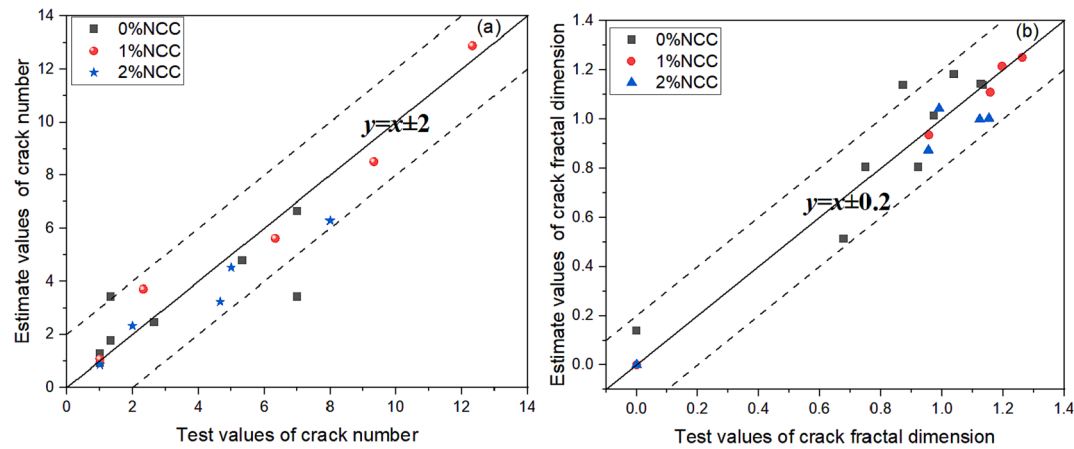


Fig. 23. Test values vs. estimate values of (a) crack number and (b) crack fractal dimension based on equations in Fig. 13.

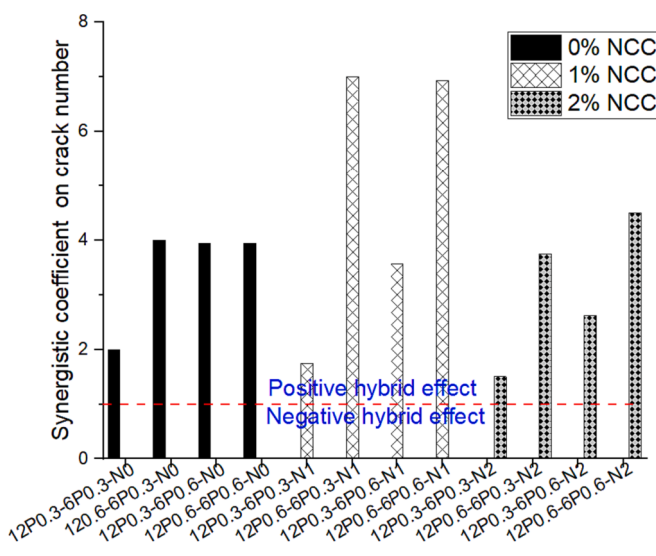


Fig. 24. Synergistic effect coefficient on crack number.

3.3.3. Synergistic effect on crack number

Synergistic effect coefficient between NCC and two lengths of PEFs on crack number is presented in Fig. 24. Same with the bending toughness, the hybrid using of 1% NCC and PEF reaches the highest synergistic effect coefficient on crack number. Compared with the individual use of PEF or NCC, the hybrid using of NCC and PEF with

different lengths can not only improve the tensile strength, but also effectively realizes the multi-crack cracking and strain hardening features of the GC, further greatly improving the toughness of the GC.

The ab initio simulation proves that Ca can improve bonding of PE and N/C-A-S-H. The SEM observation presents that 2% NCC make the GC bonding tighter with PEF than 1% NCC, consistent with the more geopolymmerization products tested by EDS. But the macro- scale toughening and multi-cracking effect of 1% NCC and PEF is better than 2% NCC and PEF on GC. The reason for this result is that the excessively strong interfacial bond of the PEF matrix will cause the PEF to break in the matrix, while the appropriate interfacial bond can make the PEF pull out from the matrix, thus consuming more energy [39]. The appropriate interfacial bond from 1% NCC make the PEF reinforced GC achieve strength criterion and energy criterion to reach strain-hardening behavior and higher toughness [52]. The other reason for the better toughening effect of 1% NCC and PEF than that of 2% NCC and PEF is due to the better dispersity of fiber in 1% NCC modified GC, as discussed in section 3.3.1.

3.3.4. Relation between crack features and bending toughness

Multi-crack development is a typical character of high and ultra-high toughness cementitious materials made of Portland cement or GC [51,53]. The quantity and width of surface cracks on high toughness cementitious material have been assessed by scholars [10,48]. Nonetheless, the complexity of cracks, such as fractal dimension, is rarely studied. Moreover, the quantitative relation between crack parameters and toughness indexes has not been studied yet.

Fig. 25 presents the relation between crack character and bending toughness. The higher crack number and fractal dimension on the

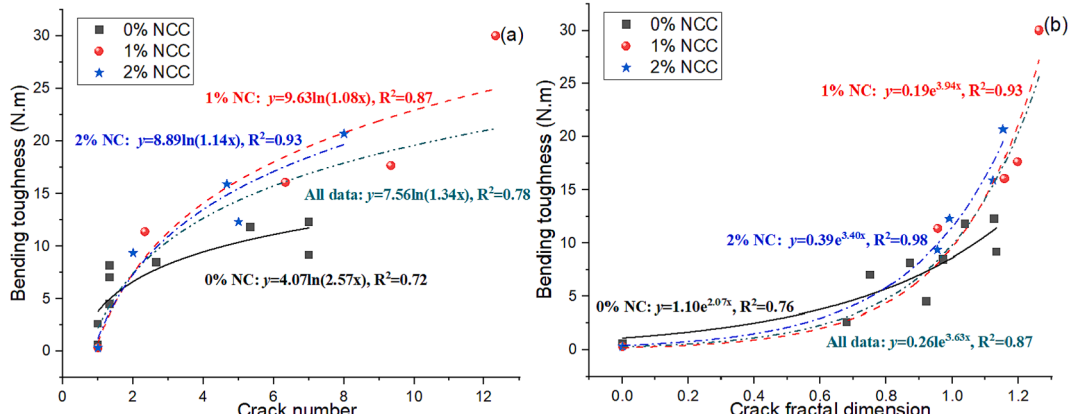


Fig. 25. Relation between (a) crack number and bending toughness, (b) crack fractal dimension and bending toughness.

Table 10

Regression ANOVA of relation between crack number and bending toughness.

	DF	Sum of Squares	Mean Square	F Value	P Value
GC with 0% NCC	1	90.82922	90.82922	18.05637	0.0038
GC with 1% NCC	1	403.82756	403.82756	20.49	0.02017
GC with 2% NCC	1	217.55963	217.55963	38.4	0.00847
All data	1	804.83627	804.83627	59.31937	0.00000061

Table 11

Regression ANOVA of relation between crack fractal dimension and bending toughness.

	DF	Sum of Squares	Mean Square	F Value	P Value
GC with 0% NCC	2	560.65945	280.32973	65.56731	2.9×10^{-5}
GC with 1% NCC	2	1569.21383	784.60691	70.92947	0.00298
GC with 2% NCC	2	915.24957	457.62479	234.09794	5.1×10^{-4}
All data	2	2975.37141	1487.68571	182.30196	3.3×10^{-12}

surface of specimen, the higher bending toughness. With the same crack number and fractal dimension, the bending toughness of PEF reinforced GC with 1% or 2% NCC is generally higher than that of PEF reinforced GC without NCC. Specifically, the bending toughness of GC mixed with 1% NCC reaches the maximum value among all specimens. The reason is that the incorporation of NCC increases the bonding strength between PEF and the GC matrix (as discussed in section 3.1 and 3.2). Hence, the PEF pull-out will consume more energy, contributing to the increase in bending toughness.

The crack number and fractal dimension have a clear positive relation with the bending toughness, as presented in Fig. 25. Most of the correlation coefficients are higher than 0.85. As shown in Table 10 and Table 11, all the P-values are less than 0.05, so the regression passes the overall significance test, regression models are meaningful. And the results of toughness estimated by the equations in Fig. 25 are all very accurate, as shown in Fig. 26. Most of the relationships between predicted and measured toughness based on crack number and fractal dimension are in the range of $y = x \pm 5$ and $y = x \pm 4$, respectively. Hence, crack number and crack fractal dimension are applicable visible indicators of the toughness of PEF reinforced GCs. Interestingly, the prediction accuracy of crack fractal dimension for bending toughness is

better than that of crack number, because crack fractal dimension can better reflect the complex random characteristics of crack development process than crack number.

Nonetheless, with the change of crack width and fractal dimension, the growth rate of bending toughness is different. Specifically, with the increase of crack number, the bending toughness has a fast increase at the beginning followed by a slow increase later. While with the increase of crack fractal dimension, the bending toughness has an opposite response (slow growth followed by rapid growth later). The relation between bending toughness and crack number tracks a good natural log function ($y = \ln(bx)$). While the relation between bending toughness and crack fractal dimension accords well with a natural exponential function ($y = ke^{bx}$). These phenomena indicate that both the number and fractal dimension of cracks can well capture the responses of bending toughness of GC although they vary in relations with the toughness. In the future, the deep learning methods could be used to obtain the crack information of high toughness GC more accurately.

4. Conclusions

The multiscale ab-initio modeling and experiment on synergistic effect of NCC and PEF on toughening GC were carried out and the conclusions could be drawn as follows:

- (1) With the introduction of Ca, the binding energies and charge transfer of CSH-PE and N/CASH-PE are significantly increased. Nonetheless, the hydrogen bonds are rarely formed with or without Ca due to the lack of polar groups of PEFs, thus contributing to the enhancement on bending toughness though PEF slip during the pull-out process.
- (2) The FTIR, TGA, SEM and EDS test indicated that NCC significantly improved micro-scale geopolymer gels aggregation on the surface of PEF, resulting from the nano-scale Ca-triggered electrostatic attractions and high bonding between N/CASH-PE.
- (3) The micro-scale NCC-induced geopolymer gels aggregation on the surface improved the bonding between PEF and GC matrix. Due to the meso-scale fiber dispersion and PEF-GC bonding, geopolymers with 12 mm + 6 mm PE fiber + 1% NCC shows the best synergistic effect on macro-scale bending toughness and multiple cracking characteristics.
- (4) The relationship of fiber reinforcing index-toughness, toughness-crack amount and toughness-crack fractal dimension tracked good linear, natural log and exponential function, respectively. The crack number and crack fractal dimension are applicable visible indicators of the bending toughness of PEF reinforced GCs.

The ab-initio modeling and micro structure test in this study proved

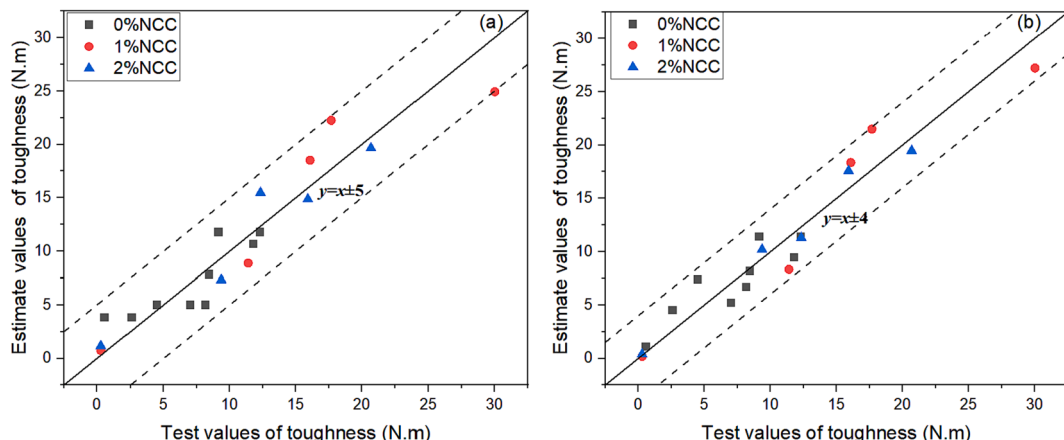


Fig. 26. Test values vs. estimate values of toughness by (a) crack number and (b) crack fractal dimension based on equations in Fig. 25.



Fig. A1. Morphologies of (a) silica fume, (b) fly ash, (c) slag, (d) silica sand, (e) NCC and (f) PEF.

that NCC improved the bonding between PEF and GC. But the single PEF pull-out test should be done in the future to obtain the accurate interface bonding strength for further mechanical properties prediction.

Declaration of Competing Interest

The authors declare that they have no known competing financial interests or personal relationships that could have appeared to influence the work reported in this paper.

Data availability

Data will be made available on request.

Acknowledgements

The National Natural Science Foundation of China (52109168) and Natural Science Basic Research Program of Shaanxi (Program No. 2021JQ-174) are gratefully acknowledged.

Appendix

Fig A

References

- [1] P. Zhang, Z. Gao, J. Wang, J. Guo, S. Hu, Y. Ling, Properties of fresh and hardened fly ash/slag based geopolymer concrete: A review, *J. Cleaner Product.* 270 (2020) 122389.
- [2] K.Z. Farhan, M.A.M. Johari, R. Demirboğa, Impact of fiber reinforcements on properties of geopolymers composites: A review, *J. Build. Eng.* 44 (2021) 102628.
- [3] Y. Ding, J. Dai, C. Shi, Fracture properties of alkali-activated slag and ordinary Portland cement concrete and mortar, *Constr. Build. Mater.* 165 (2018) 310–320.
- [4] T.T. Tran, T.M. Pham, H. Hao, Experimental and analytical investigation on flexural behaviour of ambient cured geopolymers concrete beams reinforced with steel fibers, *Eng. Struct.* 200 (2019) 109707.
- [5] A. Wetzel, B. Middendorf, Influence of silica fume on properties of fresh and hardened ultra-high performance concrete based on alkali-activated slag, *Cem. Concr. Compos.* 100 (2019) 53–59.
- [6] D. Zeng, M. Cao, The flexural behaviors and mechanism of wollastonite microfiber modified ultra-high performance concrete with steel fiber from micro to macro scale, *Arch. Civ. Mech. Eng.* 22 (1) (2022) 32.
- [7] C. Zhang, J. Liu, S. Han, Y. Hua, Pore pressure and spalling in fire-exposed high-strength self-consolidating concrete reinforced with hybrid fibres, *Eur. J. Environ. Civ. EN.* 25 (2) (2021) 337–367.
- [8] C. Zhang, C. Xia, Z. Wang, K. Zhang, Tensile properties of hybrid fiber-reinforced strain-hardening cementitious composite exposed to elevated temperature, *J. Build. Eng.* 34 (2021) 101886.
- [9] M. Cao, C. Xie, J. Guan, Fracture behavior of cement mortar reinforced by hybrid composite fiber consisting of CaCO₃ whiskers and PVA-steel hybrid fibers, *Compos. A Appl. Sci. Manuf.* 120 (2019) 172–187.
- [10] M. Cao, C. Zhang, Y. Li, J. Wei, Using Calcium carbonate whisker in hybrid fiber-reinforced cementitious composites, *J. Mater. Civil Eng.* 27 (4) (2015) 4014139.
- [11] L. Li, Y. Zhang, Y. Shi, Z. Xue, M. Cao, Surface cracking and fractal characteristics of cement paste after exposure to high temperatures, *Fractal Fract.* 6 (9) (2022) 465.
- [12] L. Li, C. Yan, N. Zhang, M.U. Farooqi, S. Xu, A.F. Deifalla, Flexural fracture parameters of polypropylene fiber reinforced geopolymers, *J. Mater. Res. Technol.* 24 (2023) 1839–1855.
- [13] L. Li, Y. Qin, M. Cao, J. Guan, C. Xie, Bending performance and calculation of reinforced beam with hybrid fiber and CaCO₃ whisker, *Comput. Concr.* 31 (3) (2023) 197–206.
- [14] J. Xiao, N. Han, Y. Li, Z. Zhang, S.P. Shah, Review of recent developments in cement composites reinforced with fibers and nanomaterials, *Front. Struct. Civ. Eng.* 15 (1) (2021) 1–19.
- [15] D. Lei, L. Guo, B. Chen, I. Curosu, V. Mechtcherine, The connection between microscopic and macroscopic properties of ultra-high strength and ultra-high ductility cementitious composites (UHS-UHDCC), *Compos. B Eng.* 164 (2019) 144–157.
- [16] Z. Wu, K.H. Khayat, C. Shi, Effect of nano-SiO₂ particles and curing time on development of fiber-matrix bond properties and microstructure of ultra-high strength concrete, *Cement Concr. Res.* 95 (2017) 247–256.
- [17] M. Saafi, L. Tang, J. Fung, M. Rahman, J. Liggat, Enhanced properties of graphene/fly ash geopolymers composite cement, *Cement Concr. Res.* 67 (2015) 292–299.
- [18] L.Y. Yang, Z.J. Jia, Y.M. Zhang, J.G. Dai, Effects of nano-TiO₂ on strength, shrinkage and microstructure of alkali activated slag pastes, *Cement Concr. Comp.* 57 (2015) 1–7.
- [19] H. Assaedi, T. Alomayri, C.R. Kaze, B.B. Jindal, S. Subaer, F. Shaikh, S. Alraddadi, Characterization and properties of geopolymers nanocomposites with different contents of nano-CaCO₃, *Constr. Build. Mater.* 252 (2020) 119137.
- [20] M.E. Gülsan, R. Alzeebaree, A.A. Rasheed, A. Niş, A.E. Kurtoglu, Development of fly ash/slag based self-compacting geopolymers concrete using nano-silica and steel fiber, *Constr. Build. Mater.* 211 (2019) 271–283.
- [21] P. Zhang, Z. Gao, J. Wang, K. Wang, Numerical modeling of rebar-matrix bond behaviors of nano-SiO₂ and PVA fiber reinforced geopolymers composites, *Ceram. Int.* 47 (8) (2021) 11727–11737.
- [22] L. Li, C. Xie, M. Cao, X. Zhou, Z. Li, Synergistic effect between CaCO₃ whisker and steel-PVA fiber cocktail in cement-based material at elevated temperature, *ASCE J. Mater. Civil Eng.* 34 (2) (2022) 4021415.
- [23] J.P. Perdew, J.A. Chevary, S.H. Vosko, K.A. Jackson, M.R. Pederson, D.J. Singh, C. Fiolhais, Atoms, molecules, solids, and surfaces - applications of the generalized gradient approximation for exchange and correlation, *Phys. Rev. B* 46 (11) (1992) 6671–6687.
- [24] J.P. Perdew, K. Burke, M. Ernzerhof, Generalized gradient approximation made simple, *Phys. Rev. Lett.* 77 (18) (1996) 3865–3868.
- [25] J. Vandevondele, M. Krack, F. Mohamed, M. Parrinello, T. Chassaing, J. Hutter, Quickstep: Fast and accurate density functional calculations using a mixed Gaussian and plane waves approach, *Comput. Phys. Commun.* 167 (2) (2005) 103–128.

- [26] G. Lippert, J. Hutter, M. Parrinello, A hybrid Gaussian and plane wave density functional scheme, *Mol. Phys.* 92 (3) (1997) 477–487.
- [27] J. VandeVondele, J. Hutter, An efficient orbital transformation method for electronic structure calculations, *J. Chem. Phys.* 118 (10) (2003) 4365–4369.
- [28] S. Goedecker, M. Teter, J. Hutter, Separable dual-space Gaussian pseudopotentials, *Phys. Rev. B Condens. Matter* 54 (3) (1996) 1703–1710.
- [29] C. Hartwigsen, S. Goedecker, J. Hutter, Relativistic separable dual-space Gaussian Pseudopotentials from H to Rn, *Phys. Rev. B* 58 (7) (1998) 3641–3662.
- [30] J. VandeVondele, J. Hutter, Gaussian basis sets for accurate calculations on molecular systems in gas and condensed phases, *J. Chem. Phys.* 127 (11) (2007).
- [31] H. Manzano, J.S. Dolado, A. Ayuela, Aluminum incorporation to dreierketten silicate chains, *J. Phys. Chem. B* 113 (9) (2009) 2832–2839.
- [32] A.K. Mohamed, P. Moutzouri, P. Berruyer, B.J. Walder, J. Siramanont, M. Harris, M. Negroni, S.C. Galmarini, S.C. Parker, K.L. Scrivener, L. Emsley, P. Bowen, The atomic-level structure of cementitious calcium aluminate silicate hydrate, *J. Am. Chem. Soc.* 142 (25) (2020) 11060–11071.
- [33] Z. Lu, J. Yu, J. Yao, D. Hou, Experimental and molecular modeling of polyethylene fiber/cement interface strengthened by graphene oxide, *Cem. Concr. Compos.* 112 (2020) 103676.
- [34] B. Nematollahi, J. Sanjayan, J. Qiu, E. Yang, High ductile behavior of a polyethylene fiber-reinforced one-part geopolymer composite: A micromechanics-based investigation, *ARCH CIV MECH ENG.* 17 (3) (2017) 555–563.
- [35] N. Sakhavand, P. Muthuramalingam, R. Shahsavari, Toughness Governs the Rupture of the Interfacial H-Bond Assemblies at a Critical Length Scale in Hybrid Materials, *Langmuir* 29 (25) (2013) 8154–8163.
- [36] J.C. Kuri, S. Majhi, P.K. Sarker, A. Mukherjee, Microstructural and non-destructive investigation of the effect of high temperature exposure on ground ferronickel slag blended fly ash geopolymers mortars, *J BUILD ENG.* 43 (2021) 103099.
- [37] A. Rafeet, R. Vinai, M. Soutsos, W. Sha, Effects of slag substitution on physical and mechanical properties of fly ash-based alkali activated binders (AABs), *Cement Concr. Res.* 122 (2019) 118–135.
- [38] M.R. Ahmad, C.S. Das, M. Khan, J.-G. Dai, Development of low-carbon alkali-activated materials solely activated by flue gas residues (FGR) waste from incineration plants, *J. Clean. Prod.* 397 (2023) 136597.
- [39] H.N. Atahan, B.Y. Pekmezci, E.Y. Tuncel, Behavior of PVA fiber-reinforced cementitious composites under static and impact flexural effects, *J Mater Civil Eng.* 25 (10) (2013) 1438–1445.
- [40] C.K. Yip, G.C. Lukey, J.S.J. van Deventer, The coexistence of geopolymeric gel and calcium silicate hydrate at the early stage of alkaline activation, *Cement Concr. Res.* 35 (9) (2005) 1688–1697.
- [41] Y. Zhang, J.W. Ju, Q. Chen, Z. Yan, H. Zhu, Z. Jiang, Characterizing and analyzing the residual interfacial behavior of steel fibers embedded into cement-based matrices after exposure to high temperatures, *Compos. B Eng.* 191 (2020) 107933.
- [42] L.e. Teng, W. Meng, K.H. Khayat, Rheology control of ultra-high-performance concrete made with different fiber contents, *Cement Concr. Res.* 138 (2020) 106222.
- [43] C. Hu, L. Li, Z. Li, Effect of fiber factor on the workability and mechanical properties of polyethylene fiber-reinforced high toughness geopolymers, *Ceram. Int.* 48 (8) (2022) 10458–10471.
- [44] J. Zhou, S. Qian, G. Ye, O. Copuroglu, K. van Breugel, V.C. Li, Improved fiber distribution and mechanical properties of engineered cementitious composites by adjusting the mixing sequence, *Cem. Concr. Compos.* 34 (3) (2012) 342–348.
- [45] M. Khan, M. Cao, M. Ali, Effect of basalt fibers on mechanical properties of calcium carbonate whisker-steel fiber reinforced concrete, *Constr. Build. Mater.* 192 (2018) 742–753.
- [46] A. Emdadi, I. Mehdipour, N.A. Libre, M. Shekarchi, Optimized workability and mechanical properties of FRCM by using fiber factor approach: theoretical and experimental study, *Mater. Struct.* 48 (4) (2015) 1149–1161.
- [47] N. Banthia, F. Majdzadeh, J. Wu, V. Bindiganavile, Fiber synergy in Hybrid Fiber Reinforced Concrete (HyFRC) in flexure and direct shear, *Cem. Concr. Compos.* 48 (2014) 91–97.
- [48] Q. Li, X. Gao, S. Xu, Multiple effects of nano-SiO₂ and hybrid fibers on properties of high toughness fiber reinforced cementitious composites with high-volume fly ash, *Cem. Concr. Compos.* 72 (2016) 201–212.
- [49] M. Sahmaran, G. Yildirim, T.K. Erdem, Self-healing capability of cementitious composites incorporating different supplementary cementitious materials, *Cem. Concr. Compos.* 35 (1) (2013) 89–101.
- [50] L.i. Li, J.-C. Tao, Y. Zhang, H.-X. Sun, K.-V. Yuen, P.-B. You, Crack fractal analysis of fractured polyethylene fiber reinforced alkali activated mortar under flexural load, *Constr. Build. Mater.* 345 (2022) 128428.
- [51] A.K. Das, C.K.Y. Leung, K.T. Wan, Application of deep convolutional neural networks for automated and rapid identification and computation of crack statistics of thin cracks in strain hardening cementitious composites (SHCCs), *Cem. Concr. Compos.* 122 (2021) 104159.
- [52] V.C. Li, Engineered Cementitious Composites (ECC): Bendable concrete for sustainable and resilient infrastructure, Springer, Berlin, Germany, 2019.
- [53] V.C. Li, F.P. Bos, K. Yu, W. McGee, T.Y. Ng, S.C. Figueiredo, K. Nefs, V. Mechcherine, V.N. Nerella, J. Pan, G.P.A.G. van Zijl, P.J. Kruger, On the emergence of 3D printable Engineered, Strain Hardening Cementitious Composites (ECC/SHCC), *Cement Concr. Res.* 132 (2020) 106038.